



Detecting Subsurface Voids From GPR Images by 3-D Convolutional Neural Network Using 2-D Finite Difference Time Domain Method

Takahiro Yamaguchi , Member, IEEE, Tsukasa Mizutani, Member, IEEE, Kimiro Meguro, and Takuichi Hirano , Senior Member, IEEE

Abstract—In this article, an algorithm for detecting subsurface voids under the road from ground penetrating radar images is proposed. A multichannel radar system mounted on vehicle enables dense and highspeed monitoring. The novelty of the algorithm is a unique ElectroMagnetic simulation method and state-of-the-art deep learning technique to consider three-dimensional (3-D) reflection patterns of voids. To train deep learning models, 3-D reflection patterns were reproduced by 2-D finite difference time domain method to drastically reduce the calculation cost. Hyperboloid reflection patterns of voids were extracted by 3-D convolutional neural network (3D-CNN). The classification accuracy of 3D-CNN was up to 90%, about 10% improvement compared to previous 2D-CNN to demonstrate the effectiveness of 3-D subsurface sensing and detection. The results were validated by real void measurement data. After applying trained 3D-CNN to radar data, regions of voids were plotted in a 3-D map, offering clear visualization of areas of voids.

Index Terms—3-D convolutional neural network (3D-CNN), deep learning, finite difference time domain (FDTD) method, ground penetrating radar (GPR), subsurface voids.

I. INTRODUCTION

ROAD collapses have been an important social issue in recent years. For example, in Japan, we have 480 000 km distance subsurface sewage pipes [1], [2]. About 5% of total distance is aged over 50 years and 40% is over 30 years, going to be 50 years in 20 years. Rapidly aging damaged pipes cause subsurface voids. Voids under the road lead to road collapses. In Japan, over 3000 road collapses occur per year, bringing devastating accidents with large financial loss to surrounding societies and endangering the safety of road users [3], [4]. Aging subsurface utilities are common issues in urban areas worldwide. Road collapses are sensationally reported in many populated cities in the United States, European and Asian countries.

Manuscript received December 14, 2021; revised January 8, 2022; accepted March 24, 2022. Date of publication April 7, 2022; date of current version May 3, 2022. (Corresponding author: Takahiro Yamaguchi.)

Takahiro Yamaguchi, Tsukasa Mizutani, and Kimiro Meguro are with the Institute of Industrial Science, University of Tokyo, Tokyo 153-8505, Japan (e-mail: tyamag@iis.u-tokyo.ac.jp; mizu-t@iis.u-tokyo.ac.jp; meguro@iis.u-tokyo.ac.jp).

Takuichi Hirano is with the Department of Electrical, Electronics, and Communication Engineering, Tokyo City University, Tokyo 158-8557, Japan (e-mail: thirano@tcu.ac.jp).

Digital Object Identifier 10.1109/JSTARS.2022.3165660

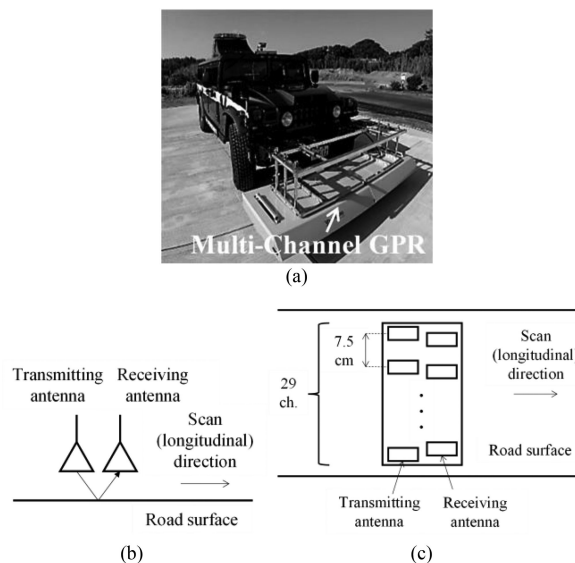


Fig. 1. Subsurface sensing under the road by GPR. (a) Typical vehicle-installed type GPR system [5]. (b) Transmitting/receiving antennas (side view). (c) Multichannel configuration (top view).

To address an increasing number of voids caused by large amounts of subsurface utilities, ground penetrating radar (GPR) mounted on a vehicle is a promising tool [see Fig. 1(a)] [5]–[11]. Other nondestructive testing (NDT) methods for subsurface void detection such as a seismic wave exploration method need traffic control and a labor of installing sensors [12], [13]. Falling weight deflectometry analyzes the stiffness of a road surface by falling a weight and measuring deflection, which also needs installation of sensors [14], [15]. An infrared camera offers a thermography of a road surface to detect the delamination of pavements, which needs the difference of temperature between day and night [16], [17]. Smaller voids in deeper regions are difficult to detect. On the other hand, GPR mounted on vehicle scans under the road highspeed, up to 80 km/h without traffic control. The resolutions in distance, channel, and depth directions of a typical very-high-frequency and ultrahigh-frequency band multichannel system in typical subsurface environment are centimeter-order. The configuration of the utilized system is shown in Fig. 1(b) and (c). The system offers dense three-dimensional (3-D) radar

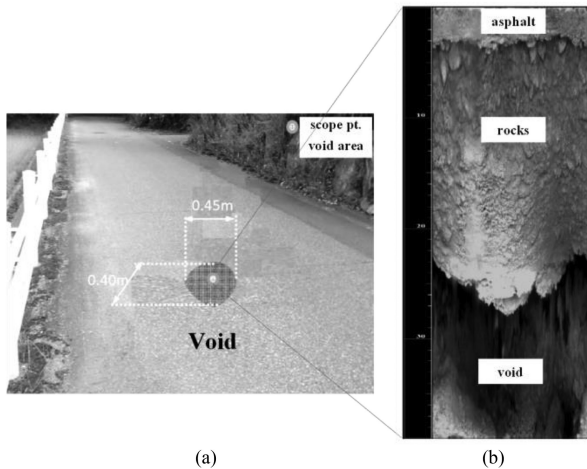


Fig. 2. Secondary survey of a void. (a) Geometry. (b) Scope image of excavated void.

data covering the target depth range of voids, 0 to 1.5 m in a 2 m single lane by one measurement.

The difficulty of GPR method is skilled inspectors manually detect reflection patterns of anomalies from each radar image. Total volume of radar data is terabyte-order, containing several to several tens kilometer distance images aligned in a channel direction. One inspection takes several months time and hundred-thousand dollar cost. An automatic detection algorithm is expected to reduce significant inspection time, cost, and labor of inspectors.

Most research works focusing on subsurface void detection by GPR are case studies and comparison with other NDT methods [18], [19]. An unanswered question is the automatic detection of voids from radar images. There are research works about the automatic detection of subsurface pipes and artificial objects [20]–[22]. The difficulty of the void detection is that it is difficult to collect large-scale measurement data of voids. Sonoda *et al.* developed a 2-D convolutional neural network (CNN) deep learning model for the classification of radar images [23], [24]. One of the ElectroMagnetic (EM) simulation methods, finite difference time domain (FDTD) method was adopted to produce void training data. The classification accuracy of conventional CNN architectures was compared changing simulation and training conditions.

The problem of the previous research is not real voids but experimental void models reproduced by stacked concrete blocks and simulation data were used for validation. The first contribution of the research is 88 real void data was extracted from radar images. A secondary survey was conducted for 35 voids, measuring the properties, e.g., depth and geometries of voids to reveal the characteristics of voids for constructing reasonable simulation models (see Fig. 2). Eighty-eight voids were, however, not enough to train deep learning models. Therefore, simulation data was utilized to increase training data. All the voids detected by inspectors were confirmed to exist by the on-site survey. There may be voids not detected by the manual inspection. The objective of the research is to propose an accurate detection algorithm to replace the labor of manual inspection.

Therefore, the inspection results were considered as a target to evaluate the developed algorithm.

Another problem is related to the achieved classification accuracy. As will be discussed in Section V, the classification accuracy of the 2D-CNN model in [23] evaluated by real voids shows about 80% classification accuracy. To conduct reliable void detection, it is a must to improve the performance of a deep learning algorithm. The idea of the research is, as a natural extension of subsurface object detection by deep CNN in the previous research works, classification accuracy was increased by utilizing the 3-D reflection patterns of voids by deep 3D-CNN. However, even by up-to-date graphics processing unit (GPU), producing hundred to thousand-order 3-D training data by 3D-FDTD is not feasible because it takes enormous calculation time and cost. The contributions are to reproduce 3-D reflection patterns by 2D-FDTD method using interpolation method and train 3D-CNN to develop an accurate void detection algorithm.

The authors applied 3D-CNN to the detection and localization of subsurface pipes [25]. The final goal of our research group is the complete reconstruction of road structures, e.g., manhole and joint covers, pavement layers, subsurface utilities and voids in an accurate and high-resolution 3-D map real-time by one radar measurement.

The rest of this article is organized as follows: Section I introduced the background and problem of the previous research. Section II summaries the contribution of the research and proposes the methodology referring to the framework of EM simulation and deep learning research. Section III denotes the configuration of the utilized system and void data. A statistical analysis of void data was conducted to construct valid simulation models. Section IV proposes the methodology to approximate 3-D reflection patterns by 2-D models and validate the reproduced patterns by 3-D patterns and responses of a real void. Section V discusses the comparison of 2-D and 3D-CNN and offers a 3-D mapping result of the real void. Section VI summarizes the findings of the research and discussions. Finally, Section VII concludes the article.

II. CONTRIBUTIONS AND PROPOSED METHODOLOGY

A. Contributions

A novel detection algorithm of subsurface voids by 3D-CNN from radar data was proposed. 3-D reflection patterns of voids were reproduced by 2D-FDTD to train 3D-CNN. To construct EM models and validate the algorithm, real void data was collected. Three contributions are listed as follows.

- 1) 88 real void measurement data was collected by a multi-channel radar system. To construct void simulation models by the FDTD method, the characteristics of 35 voids such as depth and geometries were statistically analyzed. The classification accuracy of CNN models was validated by real voids.
- 2) The methodology to simulate 3-D reflection patterns of voids by 2D-FDTD method was proposed to drastically reduce the calculation cost. The results were validated by 3-D reflection patterns produced by the 3D-FDTD method and real void measurement data.

- 3) Classification accuracy was improved by 3D-CNN to demonstrate the effectiveness of utilizing the 3-D reflection patterns of radar data.

The aim of the research is to offer a complete methodology to reproduce 3-D reflection patterns and develop an 3D-CNN model to enable accurate 3-D subsurface sensing and detection. 3-D maps were output to visualize areas of voids. Proposed Methodologies to achieve the above contributions are shown below discussing related previous research.

B. Proposed Methodology

To construct EM models, the characteristics of voids such as depth and geometries should be known. In terms of previous research about the characteristics of voids, the mechanism of the occurrence of subsurface voids was discussed by a laboratory test [3]. The research focuses on the effects of soil properties, drainage conditions, and geometries of subsurface pipes on the occurrence of voids by some case studies. In this research, the depth, positions in a lane width direction, and sizes were obtained by a secondary survey. The characteristics were statistically analyzed to derive valid EM models and produce reasonable training data. The details of the measurement configuration and analysis results were summarized in Section III by histograms.

The methodology to reproduce 3-D void reflection patterns by 2D-FDTD method was provided. Few previous research works about EM simulation methods focus on the methodology to approximate 3-D patterns by 2-D models. In the case of delamination of bridge decks, damages can be represented by 1-D layer models because delamination is homogeneous in horizontal directions [26], [27]. The reflection coefficient R of two horizontally layered media with relative permittivity $\varepsilon_1, \varepsilon_2$ and the same permeability μ_0 can theoretically be derived

$$R = \frac{\sqrt{\varepsilon_2} - \sqrt{\varepsilon_1}}{\sqrt{\varepsilon_2} + \sqrt{\varepsilon_1}}. \quad (1)$$

However, voids have 3-D geometries, where the composition of curved surfaces interacts each other.

Voids were modeled by an ellipsoid air body. The idea of the research is that the sections of a 3-D reflection pattern were approximated by 2D-FDTD models. Then, the sections were interpolated to reproduce a 3-D pattern. Considering the rotational symmetry of an ellipsoid, cylindrical coordinates were set assigning the center of voids as origin of coordinates as shown in Fig. 3. A target object is sectioned by distance r - depth z planes with angle pitch $\Delta\theta$. A 3-D model, grids, sources, and observation points are projected onto 2-D planes. 2D-FDTD is conducted in each plane. The region $I_i(r, \theta)$ between two planes $I(r, \theta_n)$ and $I(r, \theta_{n+1})$ is linearly interpolated

$$I_i(r, \theta) = \frac{\theta_{n+1} - \theta}{\Delta\theta} I(r, \theta_n) + \frac{\theta - \theta_n}{\Delta\theta} I(r, \theta_{n+1}). \quad (2)$$

In the case of a rotating body, one section is enough to reproduce the whole 3-D response. In general cases, there is a tradeoff. Smaller the $\Delta\theta$ is, the smaller interpolation error is. However, computational cost increases by decreasing $\Delta\theta$. Required $\Delta\theta$

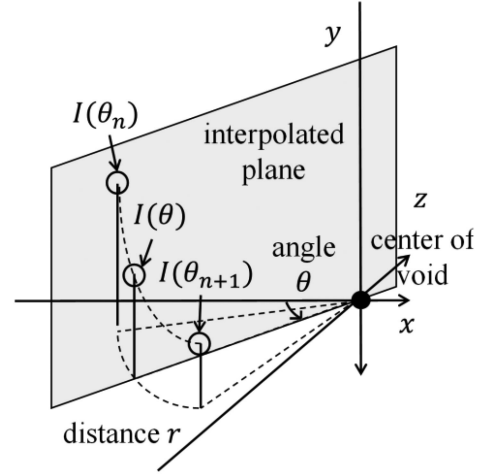


Fig. 3. Interpolation in cylindrical coordinates. In cylindrical coordinates points are a function of angle θ and distance r .

may be affected by the geometric features of objects, distance between the antennas and objects, transmitted wavelength. $\Delta\theta$ should be small enough not to affect the results. The effect of $\Delta\theta$ and interpolation accuracy of (2) were discussed in Section IV-A. Hereafter, simulated and measured waves were deconvoluted by input waves to remove the effect of waveforms of input waves. Free space loss was compensated [28]. Free space loss of 2-D and 3-D spherical waves is proportional to the distance and square of the distance, respectively.

3D-FDTD method is too heavy to compute. The required number of training data for reliable deep learning is at least thousands to several tens thousand. To produce one signal, 3-D electric and magnetic fields are iteratively calculated at each distance and time. To obtain 3-D data, a pair of transmitting and receiving antennas is moved in an observation plane point by point. It took one day to obtain one data even by a typical desktop computer and up-to-date GPU [29]. As will be discussed in Section IV-A, the proposed methodology reduced calculation time to about 0.2%, only several minutes for one data. The approximation accuracy of the methodology was evaluated considering the difference between 2-D, 3-D models, and actual void data comparing the shapes and intensities of reflection patterns.

A 3D-CNN algorithm was developed to accurately detect voids from radar data. 3D-CNN is a new horizon of deep learning research. In 3D-CNN, 3D spatial features were extracted from input 3-D data by utilizing 3-D convolution filters. 3D-CNN was utilized in medical imaging and human action recognition [30], [31]. There was no application to radar data. Ready-made model architectures are for 2D-CNN [32], [33]. In this article, to compare the performance of 2-D and 3D-CNN referring the architecture of the previous research [23], a relatively complex custom network was constructed. 3D-CNN was produced by replacing 2-D convolution filters by 3-D filters. There are numerous hyperparameters and training techniques in deep learning [34], [35]. The numbers and sizes of filters, choice of an optimization function, and training methods were confirmed not to have a large influence on classification accuracy. The details were not discussed in this article [36]. The objective

is to demonstrate the effectiveness of utilizing 3-D features of reflection patterns to accurately detect voids.

In the previous research [23], classification accuracy was increased by incorporating simulation data. In this research, 1000 simulation void data and the half of the measurement void data, 44 real voids were used for training. The other half of the measurement void data was used for validation. The same number of healthy data of simulation and measurement was prepared. The difference of simulation and real void data is it is impossible to reproduce the actual scenarios of subsurface environment, e.g., the clutters of buried objects, inhomogeneity and boundaries of soil layers and noises of systems. It is inferred that the reflection patterns of voids were learned by training data and parameters of the final classification layer were further optimized for detecting voids from real radar images. The applicability of the methodology of the research and learned parameters are discussed in Section VI. Cross validation was conducted to accurately evaluate the trained models.

Developed models were evaluated by classification accuracy (accuracy) and area under the curve (AUC) of a receiver operating characteristic curve [37], [38]. Classification accuracy is the ratio of the number of correctly classified data among the whole test data. The variation of classification accuracy and AUC of each training was 1% to 3% and 0.01 to 0.03, respectively. On the other hand, the improvements of classification accuracy and AUC of 3D-CNN compared with 2D-CNN were up to 10% and 0.1 as discussed in Section V-A. Therefore, the effectiveness of 3D-CNN was apparent.

An output was the category of void or healthy. Provided 3-D radar data, following the methodology of the previous research of Yamaguchi *et al.* [25], the whole data was searched to plot a 3-D map of possible void regions. A sliding 3-D window was moved with certain overlaps and strides in a scan and depth directions. 3D-CNN returns the probability of voids in each area. Realistic 3-D areas of voids under the road were visualized by the proposed algorithm. The achievement of the research was exhibited in Section V-B.

III. ANALYSIS OF MEASUREMENT DATA

A. Measurement System and Data

A commercial multichannel radar system shown in Fig. 1 was utilized. The number of the channels was 29. The resolution in a scanning direction was set 7 cm and a channel direction was 7.5 cm. The maximum frequency was about 3 GHz. Corresponding wavelength is about 10 cm. Larger the relative permittivity of a soil is, smaller the resolution in a depth direction becomes, possibly several centimeters considering a round trip distance. About 88 voids were collected, and 35 voids were targeted for a secondary survey. The total distance of 88 voids was about 13 km. The measurement took 10 days. Most of the sections were paved with common 5 to 7 cm asphalt layers following the Japanese standard. Soil conditions were considered to vary in 13 km sections. Therefore, the algorithm is applicable at least to standard Japanese asphalt pavement lanes measured with the same measurement system.

B. Statistical Analysis Results

The results of the secondary survey are summarized in Fig. 4. The depth of the upper surface of the voids from the road surface was measured. The channel number of the antennas where the center of the voids exists was extracted. No. 15 corresponds to the center of a driving lane and smaller number is the right side of the lane. Longitudinal (scanning direction), transverse (channel direction), and thickness (depth direction) lengths of the voids were measured. Volume was calculated by the formula of an ellipsoid body from the measured lengths. Histograms were plotted. Because the distributions were far from a gaussian distribution, median and 1 to 3 quartiles were shown for each histogram.

In terms of depth, from Fig. 4(a), the depth of the most voids was from 0.3 to 0.5 m. This may be because the most subsurface pipes exist in shallower regions. The risk of the occurrence of voids may be complex, also related to the characteristics of soils and water paths. There were few voids in regions deeper than 0.6 m. The target range of the system is from 0 to 1.5 m. Some deeper voids may be missed by the inspectors because smaller voids in deeper regions were more difficult to detect. Voids in much deeper regions below 1.5 m were not the target of GPR method. In the research, the target depth range of the simulation was assumed from 0.3 to 0.5 m.

The relative permittivity of soils can inversely be estimated from the depth of the voids and time delay of reflection patterns. The depth of a void d is calculated by the round propagation time of patterns T_d and relative permittivity of a soil ε_s assuming light velocity c [39]

$$d = \frac{1}{2} T_d \frac{c}{\sqrt{\varepsilon_s}}. \quad (3)$$

The estimated relative permittivity of the measurement data of the most voids was around 5. However, in some cases, it may be close to 3 and in other cases close to 20. The ranges of the relative permittivity and conductivity of soils were derived from the previous research [40]. For example, the range of relative permittivity was assumed to be 3 to 20. The ranges of soil properties were wide enough considering actual subsurface environment except for extreme cases such as just after rain, which can be avoided with on-vehicle systems by conducting measurement several times.

In terms of positions in a lane width direction, from Fig. 4(b), there is a tendency that most voids were in the center of a lane. Considering the loads of vehicles, the tracks of left and right tires from channel No. 5 to No. 10 and No. 20 to No. 25 should have more voids. There may be complex reasons, related to the positions of pipes, water paths, and characteristics of soils. The range of the center of the voids was assumed from channel No. 10 to No. 20.

In terms of the geometries of voids, from Fig. 4(c)–(f), the longitudinal and transverse lengths were assumed 0.5 to 1.5 m. The thickness was 0.1 to 0.2 m. The voids were flat, spreading in horizontal directions. Furthermore, the distance between the antennas and voids was significantly larger than

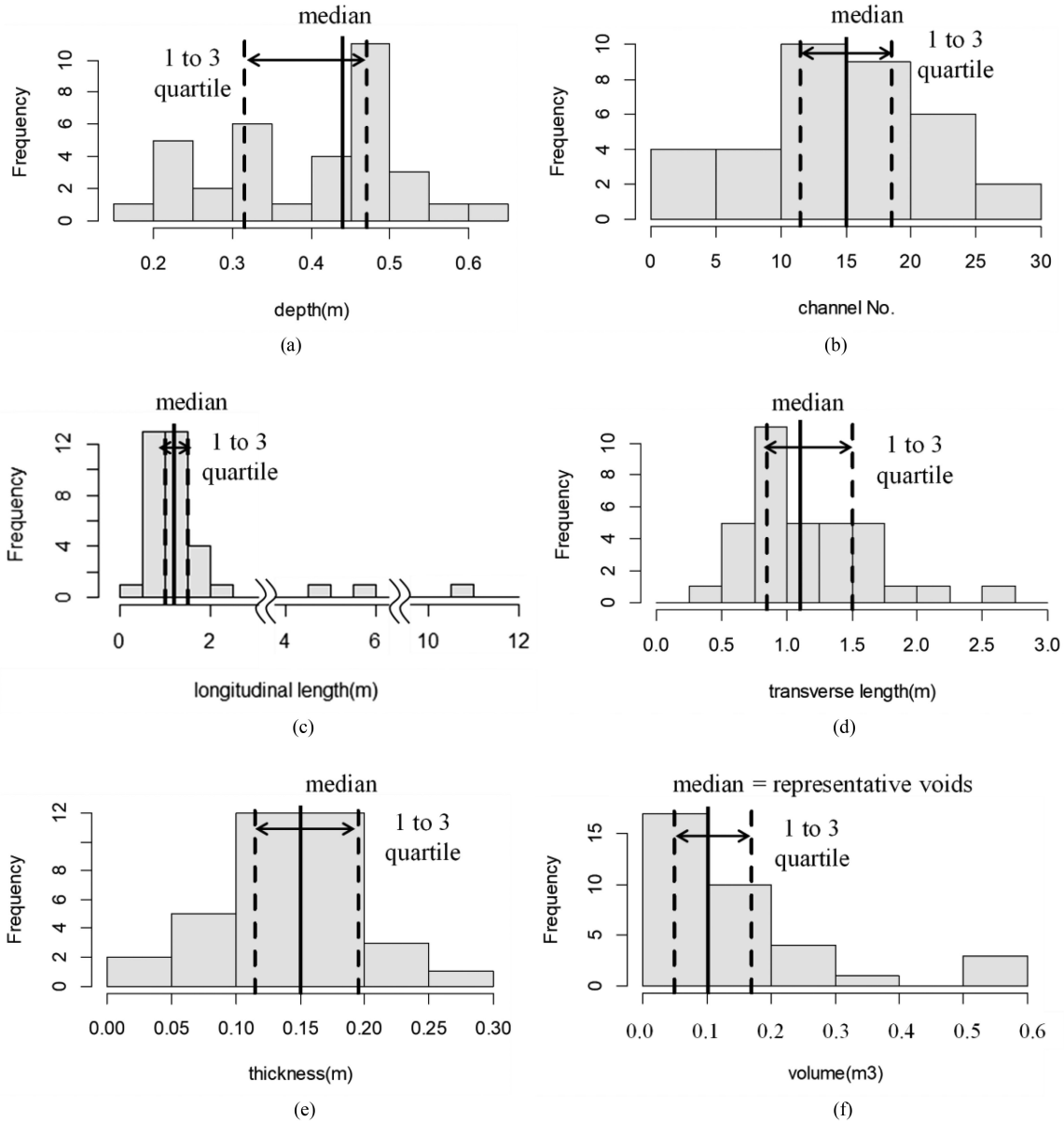


Fig. 4. Statistical analysis of secondary survey results. Positions and geometries of voids were measured. Histograms, median and 1 to 3 quartile range were plotted. (a) Depth (b) Channel No. (c) Longitudinal length. (d) Transverse length. (e) Thickness. (f) Volume.

the characteristic geometries of antennas. These two characteristics may support approximating 3-D reflection patterns by 2-D section models. If the voids had complicated 3-D geometries and close to the antennas, the 3-D propagation phenomenon and interaction between antennas and voids would not be negligible and only be reproduced by 3D-FDTD. The larger voids show almost horizontal patterns. Smaller voids were more difficult to detect. However, too small voids were not important from a practical point of view. The smallest void assumed in the research, 0.5 m by 0.5 m by 0.10 m is valid considering the practice of void detection. In terms of thickness, the upper and lower surfaces of voids were distinguishable as long as the thickness was larger than the resolution in a depth direction, which holds in an observed thickness range. The volume was concentrated in a certain range. The median of

the volume corresponds to a typical simulation void model, a 1 m by 1 m by 0.15 m ellipsoid body, supporting simulation assumptions.

C. Simulation Models

From the above discussions, as shown in Fig. 5, the parameters of depth d , thickness t , lengths a , b of void and relative permittivity ϵ_s , conductivity σ_s of soils were randomly assigned to produce 1000 training data. GPRmax was adopted as a simulation platform [41]. The effects of the unevenness of asphalt pavement thickness and inhomogeneity of soils were not considered in previous research and confirmed to be small in the context of GPR measurement by Yamaguchi [36]. The models were surrounded by an absorbing boundary condition, perfectly

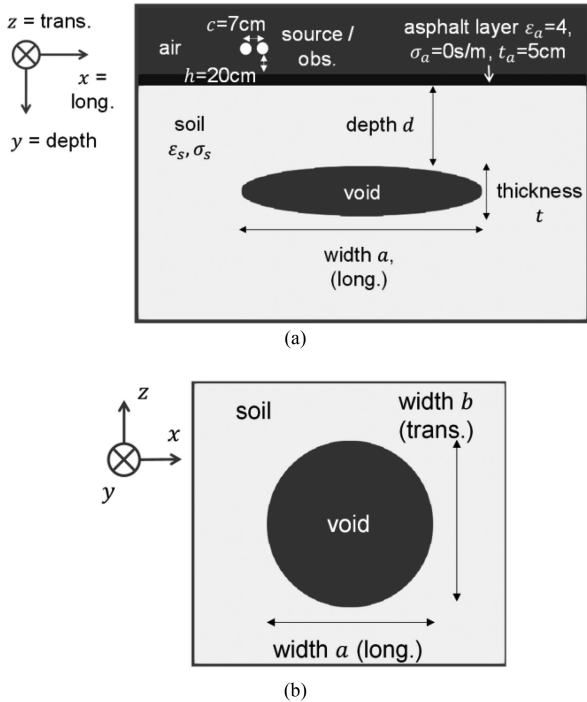


Fig. 5. Simulation void model. (a) Depth-longitudinal section. Model consists of transmitting and receiving antennas, air, asphalt and soil layers and void. (b) Horizontal section. A void was represented by an ellipsoid body.

matched layer (PML) to model infinitely large subsurface regions [42]. The thickness of PML was set to achieve enough attenuation holding continuity along boundaries. The required grid resolutions of FDTD models are determined by the wavelength of the maximum frequency of input waves and relative permittivity of media. The required time step is derived from the spatial resolution of the model by Courant—Friedrichs—Lewy condition [43].

A pair of source and observation points was moved above the road surface to model transmitting and receiving antennas. One quadrant is enough to reproduce the whole 3-D responses. Data was resampled to match the resolutions with the measurement system. The important characteristics of antennas are directivity and polarization [44], [45]. The effects of the characteristics of antennas are discussed in the Appendix. The voids were in far field and flat in horizontal directions. Therefore, the characteristics of the antennas did not have a large effect on the results. The system of Fig. 1 adopts Stepped-Frequency Continuous Wave [5], [46]. The radar transmits a signal with a certain frequency at a given time range modulating frequencies. In the simulation, a measured transmitting waveform from 50 MHz to 3 GHz of the utilized system was input as a time history of voltage. The produced training data models radar data obtained by the system.

The randomness of the characteristics of voids and soils has complex effects on simulated reflection patterns. Examples are shown in Fig. 6. As shown in Fig. 6(a) and (b), typical patterns are the positive and negative hyperbolics of upper and lower surfaces of voids. As shown in Fig. 6(c) and (d), the larger the depth of voids and relative permittivity of soils are, larger the time delay of patterns becomes. Fig. 6(e) and (f) display the length and thickness of voids affect the shape of hyperbolic patterns.

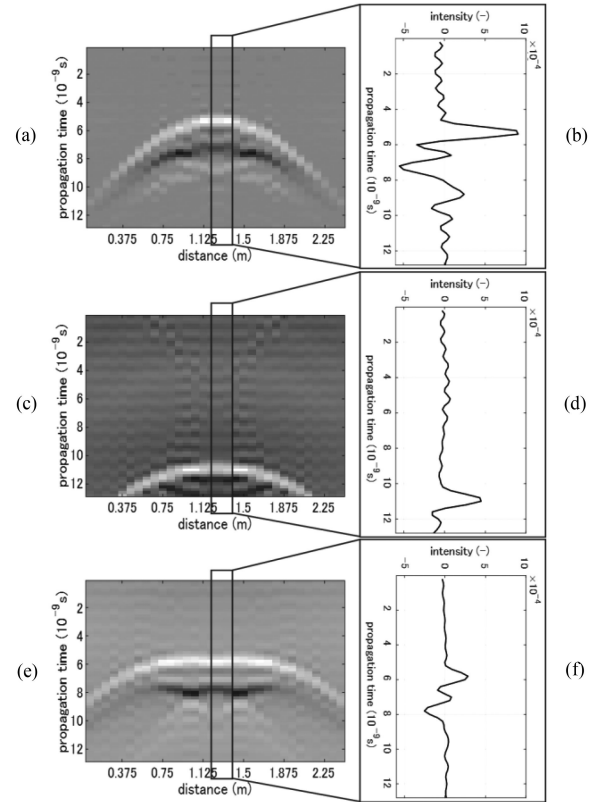


Fig. 6. Examples of simulated training data. (a), (c), (e) Vertical sections of reflection patterns. White is positive and black is negative electric field intensity. (b), (d), (f) Waveforms.

TABLE I
RANDOMNESS OF SIMULATION VOID MODEL

Parameter	Variation	
Soil	Relative permittivity ϵ_s (-)	3 - 20
	Conductivity σ_s (S/m)	0.001 - 0.01
Void	depth d (m)	0.3 - 0.5
	width a (long., m)	1.0 - 1.5
	width b (trans., m)	0.5 - 1.5
	thickness t (m)	0.1 - 0.2

Larger the length and smaller the thickness are, smaller the slopes of hyperbolics become. Intensities are mainly affected by the relative permittivity and conductivity of soils. The shapes of patterns were various as shown in Fig. 6. Time delay and intensity have at most 50% variations by the provided conditions of Table I, which is consistent with the intuition of practitioners.

IV. REPRODUCING 3-D PATTERNS BY 2D-FDTD METHOD

In Section II-B, the methodology to reproduce the 3-D reflection patterns of voids by 2D-FDTD method was introduced. The three possible sources of errors of reproduced 3-D reflection patterns were considered: interpolation error by (1) which depends

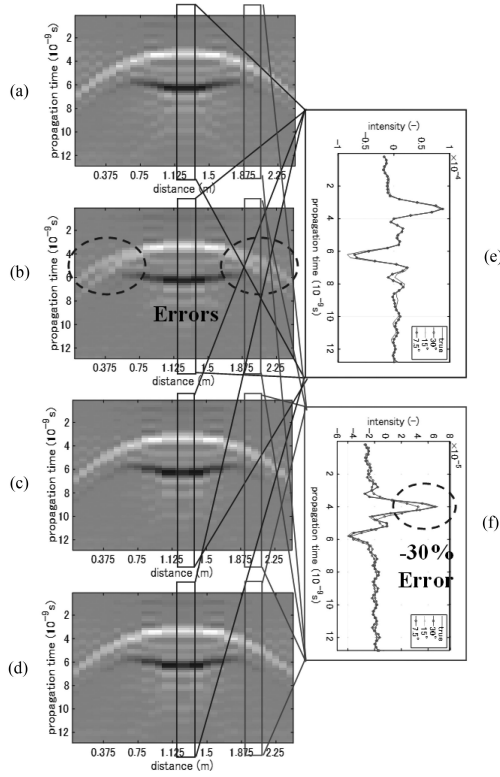


Fig. 7. Effect of angle pitch $\Delta\theta$. (a) True reflection pattern at $\theta = 45^\circ$. (b), (c), (d) Interpolated patterns with $\Delta\theta = 30^\circ$, 15° , 7.5° , respectively. (e), (f) Comparison of 1/2nd and 1/4th point waveforms of patterns.

on angle pitch $\Delta\theta$; approximating 3-D patterns by 2-D models; modeling real voids by EM models. The discussions follow one by one in this section. As a typical case, $\varepsilon_s = 5$, $\sigma_s = 0.005$ S/m, and $d = 0.5$ m were considered. Tendency was similar with other parameters. The methodology is to approximate 3-D models by 2-D section models at each angle in cylindrical coordinates. When a and b are the same, the interpolation error of rotational body is zero. Considering the most severe case, $a = 1.5$ m, $b = 0.5$ m, and $t = 0.20$ m were assumed below.

A. Error by Interpolation

Fig. 7 shows the effect of $\Delta\theta$. $\theta = 0^\circ$ corresponds to a longitudinal direction and $\theta = 90^\circ$ to a transverse direction. Interpolated reflection patterns at $\theta = 45^\circ$ when $\Delta\theta = 30^\circ$, 15° , 7.5° and true pattern were compared. B-scan was constructed extracting closest grid points to target section plane θ . The reflection patterns were compared by the shapes and intensities of patterns. The comparison of the true pattern at $\theta = 45^\circ$ and interpolated patterns at each $\Delta\theta$ is shown in Fig. 7(a)–(d). White is positive electric field intensity and black is negative. Fig. 7(e) and (f) show the comparison of waveforms at a 1/2nd (center) point, and 1/4th point. The 1/2nd point is slightly shifted from the center of a void to compare interpolated sections. The 1/4th point is 0.5 m distant from the center. The absolute peak values of the 1/2nd and 1/4th points are compared in Table II. At the 1/2nd point, a positive peak of an upper surface of a void and negative peak of a lower surface were observed. At the

TABLE II
EFFECT OF ANGLE PITCH ON PEAK VALUES OF WAVEFORMS

Angle pitch $\Delta\theta$	1/2nd waveform		1/4th waveform	
	1st peak (error %)	2nd peak (error %)	1st peak (error %)	2nd peak (error %)
30°	+4.4	-15.9	-31.2	+14.7
15°	+4.4	-15.9	-6.8	+8.8
7.5° (proposed)	+4.4	-15.9	-4.6	+8.8

TABLE III
COMPARISON OF PEAK VALUES OF PROPOSED METHOD AND TRUE PATTERNS

Angle θ	1/2nd waveform		1/4th waveform	
	1st peak (error %)	2nd peak (error %)	1st peak (error %)	2nd peak (error %)
0°	-9.1	-18.8	+21.2	+8.9
45°	-13.4	-18.5	+12.2	+2.2
90°	+6.7	+0.8	-8.4	(-)

1/4th point, a negative peak was smaller than a positive peak. The errors of the four peaks were summarized.

An interpolated pattern at $\Delta\theta = 30^\circ$ shows a large error as shown in Fig. 7(b), in which a false pattern appears. The largest error of the peak values was about 30% as shown in Table II. Smaller $\Delta\theta$ was, an interpolation error became smaller. Theoretically speaking, when $\Delta\theta$ becomes infinitely small, the error converges to zero. However, calculation cost is also an important point. 2D-FDTD in one section to obtain one image takes several tens seconds with GPU. At $\Delta\theta = 15^\circ$, it takes several minutes to obtain one data. Calculation time is reduced to about 0.2% compared to 3D-FDTD, indicating the powerfulness of the proposed methodology. In the following discussions, $\Delta\theta = 15^\circ$ was adopted.

The error caused by interpolation may theoretically be expected. Considering an ellipse with 1.5 m semimajor axis length and 0.5 m semiminor axis length, the radius L at $\theta = 45^\circ$ and neighboring sections can be calculated. The difference of the radii, interpolation error is 8 cm at $\Delta\theta = 30^\circ$, while 2 cm at $\Delta\theta = 15^\circ$ and 1 cm at $\Delta\theta = 7.5^\circ$. The horizontal resolutions of the data were about 10 cm, comparable with the case $\Delta\theta = 30^\circ$ while much larger than interpolation error at $\Delta\theta = 15^\circ$ and $\Delta\theta = 7.5^\circ$, in which the interpolation error was not important and not expected to affect the results.

B. Error by Approximating 3-D Patterns by 2-D Models

The previous section discussed the error caused by interpolation. The error of approximating 3-D models by 2D-FDTD method after appropriate interpolation was shown in Fig. 8. The reflection patterns of 3D-FDTD and 2D-FDTD at $\theta = 0^\circ$, $\theta = 45^\circ$ and $\theta = 90^\circ$ are shown in Fig. 8(b), (c), (f), (g), (j), and (k). The comparison of waveforms at 1/2nd and 1/4th points is shown in Fig. 7(d), (e), (h), (i), (l), and (m). In Table III, all the peak values were compared. In Fig. 8(m), because of the geometry of the void, clear negative peaks were not observed. Therefore, 2nd peaks at the 1/4th point were not compared.

From Fig. 8, in all the sections, 3-D responses were well reproduced in terms of the shapes and intensities of patterns.

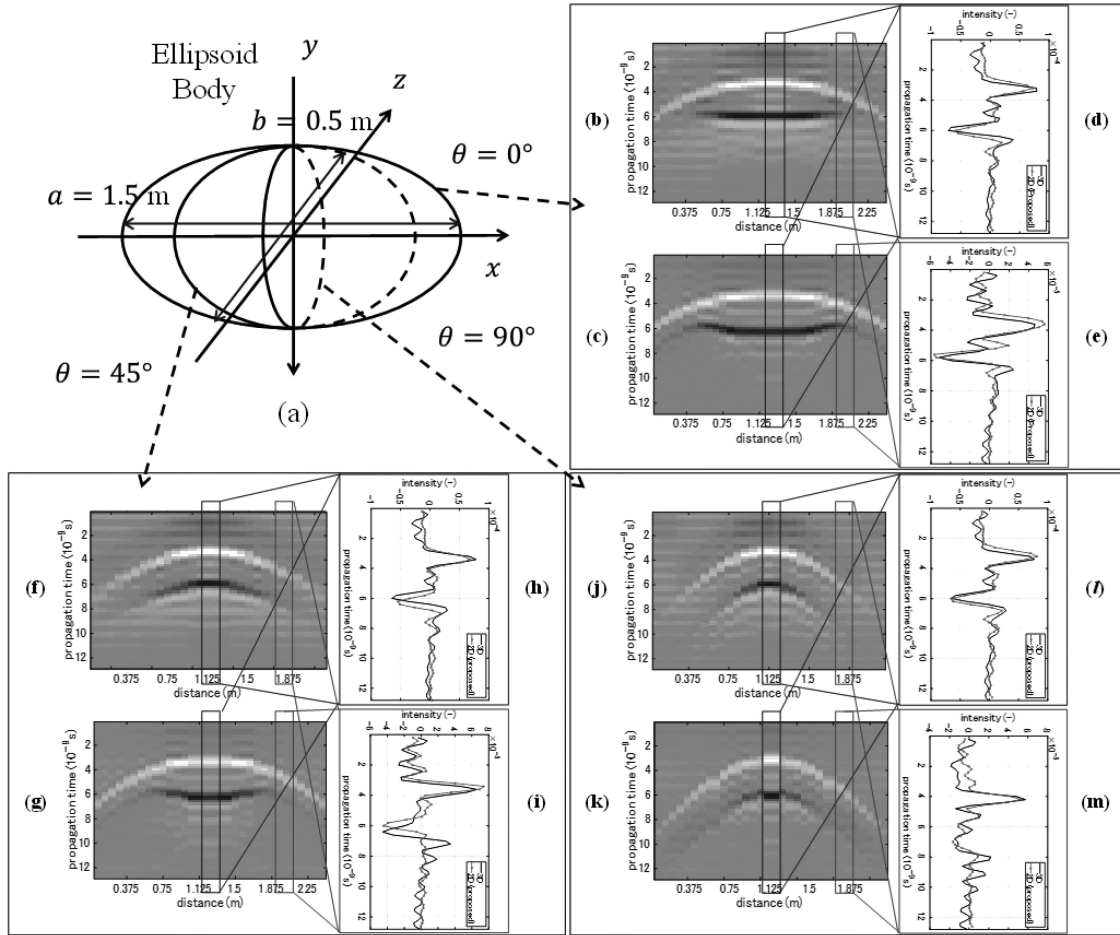


Fig. 8. Comparison of proposed method and 3D reflection patterns. (a) Assumed ellipsoid model. (b), (c), (f), (g), (j), (k) Vertical sections of reflection patterns at $\theta = 0^\circ, 45^\circ, 90^\circ$, respectively. Top figures are true patterns of the 3-D model and bottom figures are the proposed method. (d), (e), (h), (i), (l), (m) 1/2nd and 1/4th point waveforms of each pattern.

The effect of approximating by 2-D models was small. The errors of the peak values were at most 20%. Considering the intensities of patterns can be doubled or halved depending on the characteristics of surrounding soils as discussed in Section III-C, the proposed method was accurate.

The method approximates 3-D models in a radial direction. The method is not favorable for elongated objects such as subsurface pipes, in whose case 2D-FDTD method in perpendicular sections is more appropriate. Very complex 3-D geometric features may cause a large error. With the assumed frequency range and geometries of target objects, the approximation is allowable from the results.

C. Error By Approximating Real Voids By EM Models

The method was also validated by a real measured void pattern. Fig. 9 shows the comparison of measured and simulated reflection patterns and waveforms. The depth d , longitudinal length a , transverse length b , and thickness t of the target void were 0.45, 1, 0.5, and 0.3 m. The relative permittivity $\epsilon_s = 5$ and conductivity $\sigma_s = 0.005$ of a soil were considered. From the results, the reflection patterns of the void were well reproduced by the proposed method. The largest errors of the peak values were 20% from Table IV, which is consistent with

TABLE IV
COMPARISON OF PEAK VALUES OF THE PROPOSED METHOD AND REAL VOID

	1/2nd waveform		1/4th waveform peak (error %)
	1st peak (error %)	2nd peak (error %)	
simulated	+10.9	+18.7	-16.5

the results of Table III. However, the measured radar image was noisy as shown in Fig. 9(a) possibly because of clutters of other embedded objects, boundaries of soil layers, and noises of the measurement system. Accurately reproducing these on-site clutters and noises is difficult. Simulation data was used to increase measurement data by simulating void patterns.

V. DEVELOPMENT OF 3D-CNN DETECTION ALGORITHM

A. Comparison of 2-D and 3D-CNN

Simulated 3-D data was utilized to train a 3D-CNN model for void detection. Deep 2-D and 3D-CNN models were constructed to compare classification accuracy. The code was written in Tensorflow [47]. Fig. 10 shows the proposed 3D-CNN model. The model consists of four convolution and two fully connected layers to output the probability of categories, void or healthy

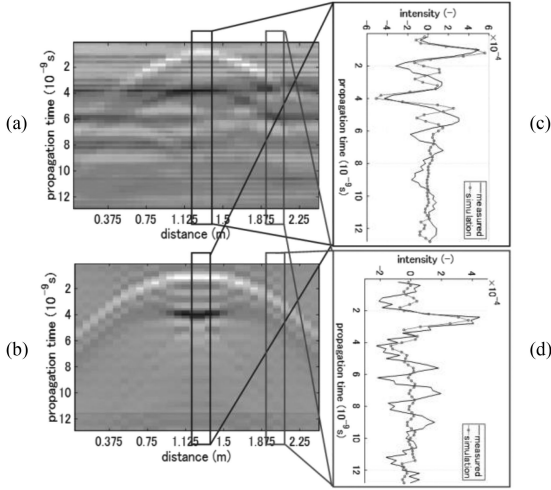


Fig. 9. Comparison of proposed method and real void patterns. (a) Measured pattern. (b) Reproduced simulation pattern. (c), (d) Comparison of 1/2nd and 1/4th point waveforms.

TABLE V
COMPARISON OF PERFORMANCE OF 2-D AND 3D-CNN

Model	Accuracy (%)	Precision (%)	Recall (%)	AUC (-)
2D-CNN	78.8	75.5	82.0	0.79
3D-CNN (proposed)	87.3 (+8.5)	91.6 (+16.1)	81.4 (-0.6)	0.91 (+0.12)

by the final softmax layer. A 2D-CNN model was produced by removing the third dimension of the input data and convolution filters. Readymade models are for 2D-CNN. The model is based on the previous research to demonstrate the effectiveness of 3D-CNN [23]. 3D-CNN utilizes all the 29 channels to extract the 3-D features of the input data. There are many hyperparameters and training techniques in deep learning. The numbers and sizes of the convolution filters and sizes of fully connected layers were optimized. There is a tendency that classification accuracy converges at certain numbers and sizes. Categorical cross-entropy was used for an objective function. Early stopping, learning rate decay, and momentum was not adopted because training time was relatively small. Training was manually stopped within 1% validation accuracy improvement after ten steps, about several tens minutes for one training by typical GPU environment [29].

3D-CNN improves the performance. Table V summarizes the performance of the developed models on 44 real voids. From the results, the accuracy of 2D-CNN was about 80% and AUC was about 0.8. On the other hand, the accuracy of 3D-CNN was about 90%, by 10% increase. AUC was about 0.9, by 0.1 increase. In practice, the detection rate of skilled inspectors is said to be around 80%, implying the achieved accuracy was high from a practical point of view. 3D-CNN utilizes the 3-D features of the input data to accurately detect voids from spurious and noisy background images. The authors confirmed accuracy decreased by about 6% by replacing 3-D convolution filters by 2-D filters while the same 3-D data was input. The typical

TABLE VI
EFFECT OF DIRECTIVITY OF ARRAY ANTENNA MODEL

	1/2nd waveform		1/4th waveform	
	1st peak (error %)	2nd peak (error %)	1st peak (error %)	2nd peak (error %)
simulated	+9.0	+12.5	+6.7	-0.5

reflection pattern of a void is a hyperboloid. 3-D filters effectively learn 3-D features to increase accuracy.

Fig. 11 shows the examples of the detected reflection patterns of voids. Fig. 11(a) and (b) were detected by both 2-D and 3D-CNN algorithms. From Fig. 11(a), the positive and negative hyperbolic reflection patterns of a void was apparent. Fig. 11(c) and (d) were detected only by the 3D-CNN. From Fig. 11(c), an anomaly is observed though the reflection pattern is irregular. In some cases, a certain portion of a pattern was missing, not showing a complete symmetric pattern. 3D-CNN accurately detects voids by considering 3-D reflection patterns. Fig. 11(e) and (f) show the patterns not detected even by 3D-CNN. Most of the undetected voids may did not show clear patterns. For a future work, further case studies are considered collecting large-scale data. The achieved classification accuracy of 3D-CNN was reasonable.

B. 3-D Mapping of Voids

The developed 3D-CNN algorithm is applied to the whole radar data to plot 3-D maps of voids. 3D-CNN returns the probability of each category, void or healthy for each 3-D region. An appropriate localization scheme is needed. Box-by-box search was adopted in the research [25]. The method was proposed by the authors for the detection of subsurface pipes by 3D-CNN. The whole data was searched one region after another by shifting a 3D window. Overlaps are applied, which are the ratios of the overlapped lengths in scan and depth directions to the sizes of the 3D region. Overlaps and threshold of probability of voids are the parameters.

Fig. 12 shows the example of the detection result of a void. Faithfully following the parameters of the previous research [25], probability threshold $P = 0.995$, and overlaps $OL = 75\%$ were assigned. The tendency was the same with other radar data. It is suggested parameters may further be optimized by large-scale data for different targets, subsurface pipes, and voids. The parameters were applicable to any radar data with the same measurement system. Appropriate P may be changed considering the acceptable rate of missing voids. Fig. 12(a) and (b) display the configuration of the void. The boxes in Fig. 12(c) show detected regions. In Fig. 12(c), the void was successfully detected and shown in the 3-D map by the corresponding areas. The sizes of boxes are 1 m depth by 2 m longitudinal direction length by 2 m transverse direction length, which can localize areas and visualize voids in 3-D maps. Two boxes were successively detected in a depth direction because the void was between the two regions.

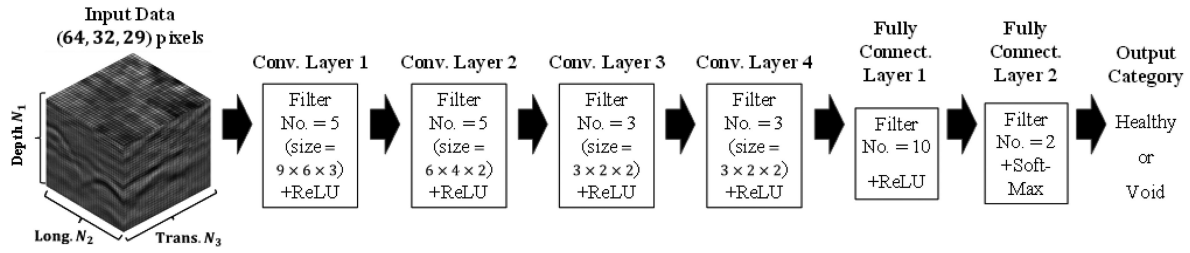


Fig. 10. Configuration of deep 3D-CNN model. Model is composed of four convolution and two fully connected layers [23]. 2D-CNN was made by replacing 3-D filters of convolution layers by 2-D filters.

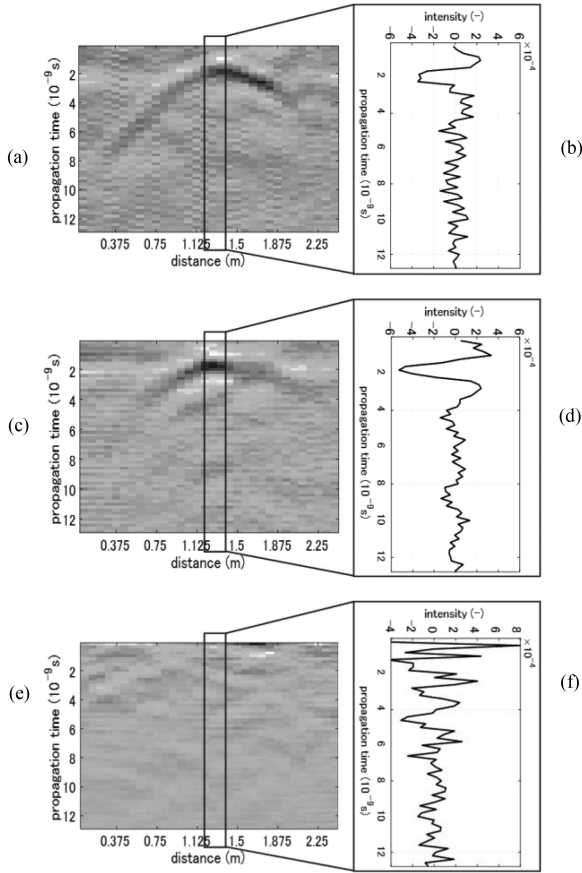


Fig. 11. Examples of detected void reflection patterns. (a) Detected by 2D-CNN. (b) Detected only by 3D-CNN. (c) Not detected even by 3D-CNN.

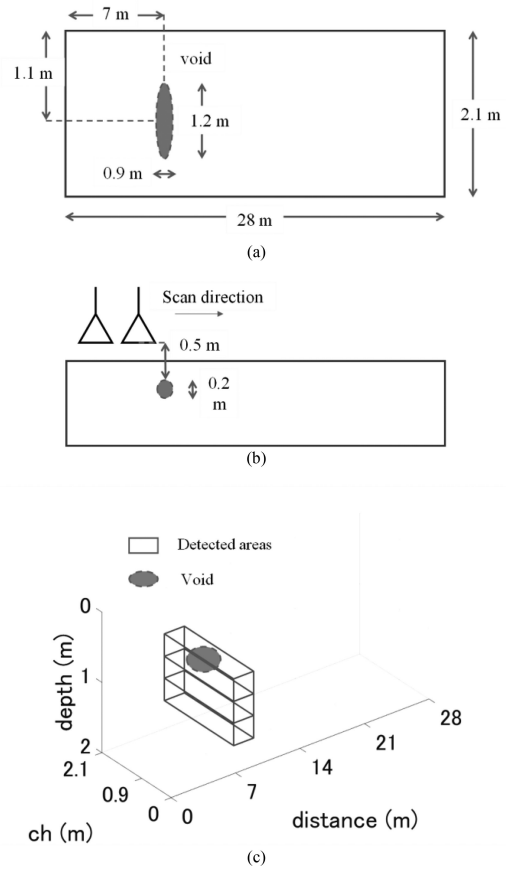


Fig. 12. Configuration of real void and result of proposed mapping algorithm. (a) Top view of position of void. (b) Side view. (c) 3-D mapping result.

TABLE VII
EFFECT OF DIRECTION OF ANTENNA POLARIZATION

Angle θ	1/2nd waveform		1/4th waveform	
	1st peak (error %)	2nd peak (error %)	1st peak (error %)	2nd peak (error %)
90°	-9.5	+3.5	-13.9	+14.2

VI. FINDINGS AND DISCUSSIONS

3-D reflection patterns of voids were reproduced by 2D-FDTD method to train 3D-CNN. The effectiveness of 3-D subsurface sensing and detection by GPR was demonstrated by comparing the classification accuracy of 2-D and 3D-CNN.

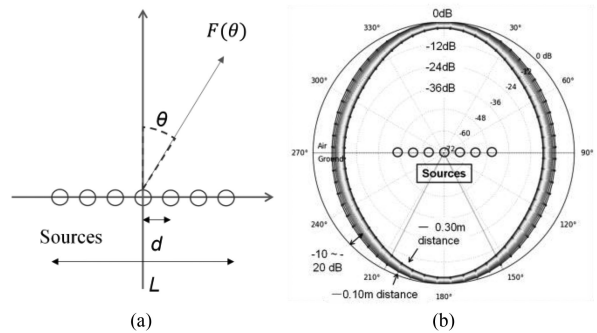


Fig. 13. Directivity of array antenna. (a) Configuration of the model. (b) Directivity of the model. If there is one point source, a nondirectional feature would be shown.

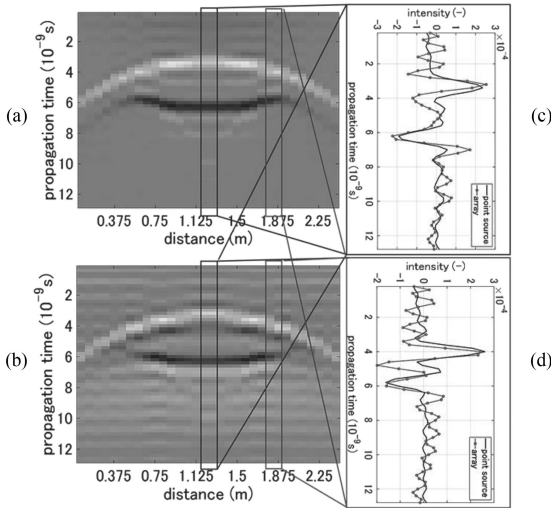


Fig. 14. Comparison of adopted point source and array antenna models. (a) Reflection pattern of point source. (b) Array antenna. (c), (d) Comparison of 1/2nd and 1/4th point waveforms.

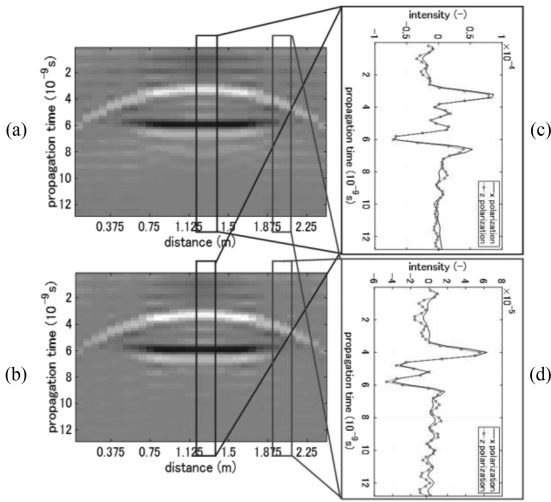


Fig. 15. Comparison of z-polarization (perpendicular, adopted) and x-polarization (longitudinal) antennas. (a) Reflection pattern of z-polarization. (b) x-polarization. (c), (d) Comparison of 1/2nd and 1/4th point waveforms.

A 3-D map of a void was plotted to visualize the area of the void. The findings were summarized as follows.

- 1) Radar data of real voids was collected by a commercial multichannel radar system and a secondary excavation survey was conducted. The voids were flat. The shape can be represented by an ellipsoid body of air. The ranges of soil properties were derived from the previous research. Parameters were randomly assigned to produce training void data with various reflection patterns.
- 2) The methodology to reproduce the 3-D reflection patterns of voids by 2D-FDTD method was proposed. Considering an ellipsoid body, the patterns were approximated by 2-D section models and interpolated in cylindrical coordinates. Calculation time is reduced to about 0.2% compared to 3D-FDTD, showing the effectiveness of the

proposed methodology, which was also validated by the measurement void data.

- 3) A 3D-CNN custom deep learning model was constructed to compare the performance with 2D-CNN. 3D-CNN utilizes all the 29 channels of input data and 3-D convolution filters to extract 3-D features. The classification accuracy of 3D-CNN of 44 real voids was about 90%, by 10% increase compared with 2D-CNN. AUC was about 0.9, by 0.1 increase. The void was successfully detected and localized in a 3-D map by the areas of boxes after box-by-box search.

The advantage of the research is the high accuracy of 3-D subsurface sensing and detection. A 3-D map was output, which is impactful for practitioners. In terms of the limitation of the research, the assumed EM void models were based on large-scale measurement data. Therefore, the algorithm is applicable at least to standard Japanese road measured by the same system. The methodology may further be demonstrated by other large-scale measurement data obtained by other systems. False detection and missing cases may further be investigated to increase classification accuracy. For a future work, the depth, thickness, and sizes of voids may be inversely estimated from radar images to help road administrators evaluate integrality and plan repair works.

VII. CONCLUSION

In this article, we proposed a novel subsurface void detection algorithm from radar images based on 3D-CNN (AI) and 2D-FDTD method (EM simulation). 3-D reflection patterns were reproduced by 2D-FDTD method by interpolating section models in cylindrical coordinates. Calculation cost was drastically reduced by the proposed method. Patterns of voids were detected by 3D-CNN utilizing 3-D spatial features of input data by 3-D convolution filters. The classification accuracy of 3D-CNN was about 90%, about 10% increase compared with conventional 2D-CNN. The algorithm was validated by real void measurement data. Areas of the void were plotted in a 3-D map to visualize the void. The effectiveness of 3-D subsurface sensing and detection was demonstrated.

For future works, the algorithm may further be validated by other large-scale measurement data obtained by other systems. False detection and missing cases may further be investigated to increase classification accuracy. The depth, thickness, and sizes of voids may be inversely estimated from radar images. The achievement of the research was by a relatively simple deep 3D-CNN architecture, the best performance was obtained to enable practical void detection in a real road environment. Other deep learning and region proposal approaches such as R-CNN and YOLO may be considered to advance our detection algorithm.

APPENDIX

Directivity and direction of polarization of antennas are important parameters in the context of antenna designing and EM simulations. There are few research works about the effects of characteristics of GPR antennas on subsurface object detection.

The conclusion is that the effects are small in the context of subsurface void detection by the provided measurement conditions and environment.

In the research, the effect of directivity is considered by an array antenna model [48]. Fig. 13 shows the array antenna model. The directivity was reproduced by N point sources aligned in a scanning direction. The parameters are the length of the antenna L and interval d . The relationship $L = (N - 1) d$ holds. Assuming an intensity, phase delay, and antenna pattern of sources are the same W , electric field intensity $E(r, \theta)$ in polar coordinates caused by a source i at distance r_i is written by a wave number k_0

$$E(r, \theta) = W \cdot AF(\theta) \cdot \frac{\exp(-jk_0 r)}{|r|}. \quad (4)$$

AF is an array factor and written by the function of angle θ

$$AF(\theta) = \sum_{i=1}^N \exp\left(jk_0 \frac{r}{|r|} \cdot r_i\right). \quad (5)$$

AF represents the directivity of the array antenna. Larger the L is, the stronger the directivity is. Considering the directivity of the utilized system, $L = 12$ cm was adopted. As shown in Fig. 13(b), the power decreases by 10 to 20 dB at a $\theta = 45^\circ$ direction compared with directly below the antennas.

The peak values of waveforms were similar irrespective of the directivity. Fig. 14 shows the effect of directivity on the reflection patterns and waveforms. A 2-D model assuming the case of Fig. 8(b)–(d) at $\theta = 0^\circ$ was considered here. No directivity was considered in a perpendicular direction referring to the characteristics of utilized antennas. If there is one point source, no directivity was shown. From Table VI, the differences of absolute peak values compared with the case of no directivity were at most 13%, indicating the effect is small. The voids were in a far field. The characteristic sizes of the antenna were small compared with the geometries of voids. A relatively large ringing effect was observed around the void pattern because of the interaction between aligned point sources. The characteristics of sources were considered by inputting measured impulse waves. In terms of directivity, a point source is accurate enough to approximate the antennas.

Polarization direction is a critical issue in the case of 3-D objects elongated in a certain direction such as a subsurface pipe. However, in the case of subsurface voids targeted in the research, the effect of polarization direction is small. Fig. 15 shows the comparison of reflection patterns with each polarization direction in the case of Fig. 8(b)–(d) at $\theta = 0^\circ$. z-direction corresponding to a transverse direction was compared with x-direction corresponding to a longitudinal direction. The geometries in a perpendicular direction to the model affect the results. From Fig. 15 and Table VII, regardless of the polarization direction, differences were small because of the flat geometries of the void. A usual commercialized GPR system detects a subsurface pipe extended in both the longitudinal and transverse directions, implying intermediate polarization characteristics. In this article z-direction polarization is considered in 3D-FDTD cases. In 2D-FDTD cases, a polarization direction is always perpendicular to simulated sections. The error of

approximating 3-D models by 2-D section models was partly from assuming the polarization direction is perpendicular to the models.

ACKNOWLEDGMENT

The authors would like to thank the related persons of C. E. Management Integrated Laboratory Co., Ltd., Nagano prefecture, Japan, and Fujimura Crest Co., Ltd., Niigata prefecture, Japan, for the help for the research.

REFERENCES

- [1] Ministry of Land, Infrastructure, Transport and Tourism, "Maintenance and management of sewage pipe (in Japanese)," Japan. Accessed: Nov. 1, 2021. [Online]. Available: http://www.mlit.go.jp/mizukokudo/sewage/crd_sewage_tk_000135.html
- [2] Ministry of Land, Infrastructure, Transport and Tourism, "Statistics about road (in Japanese)," Japan. Accessed: Nov. 1, 2021. [Online]. Available: https://www.mlit.go.jp/road/soudan/soudan_10.html
- [3] M. Sato and R. Kuwano, "Influence of location of subsurface structures on development of underground cavities induced by internal erosion," *Soils Foundations*, vol. 55, no. 4, pp. 829–840, 2015.
- [4] A. Shimbun, "30 m road collapse at Hakata station (in Japanese)," Japan. Accessed: Nov. 1, 2021. [Online]. Available: <https://www.asahi.com/articles/ASJC82Q11JC8TIPE002.html>
- [5] 3D Radar, "3D-Radar," Norway. Accessed: Nov. 1, 2021. [Online]. Available: www.3d-radar.com
- [6] D. J. Daniels, *Ground Penetrating Radar*, 2nd ed. London, U.K.: Inst. Eng. Technol., 2004.
- [7] H. M. Jol, *Ground Penetrating Radar Theory and Applications*, 1st ed. Oxford, U.K.: Elsevier, 2009.
- [8] J. Hugenschmidt, "Concrete bridge inspection with a mobile GPR system," *Construction Building Mater.*, vol. 16, no. 3, pp. 147–154, 2002.
- [9] S. Zhao and I. L. Al-Qadi, "Development of regularization methods on simulated ground-penetrating radar signals to predict thin asphalt overlay thickness," *Signal Process.*, vol. 132, pp. 261–271, 2015.
- [10] A. Benedetto, F. Tosti, L. B. Ciampoli, and F. D'Amico, "An overview of ground-penetrating radar signal processing techniques for road inspections," *Signal Process.*, vol. 132, pp. 201–209, 2017.
- [11] H. Zhou, M. Sato, and H. Liu, "Migration velocity analysis and prestack migration of common-transmitter GPR data," *IEEE Trans. Geosci. Remote Sens.*, vol. 43, no. 1, pp. 86–91, Jan. 2005.
- [12] M. Ge, H. Wang, H. R. Hardy, Jr., and R. Ramani, "Void detection at an anthracite mine using an in-seam seismic method," *Int. J. Coal Geol.*, vol. 73, no. 3/4, pp. 201–212, 2008.
- [13] G. Grandjeana and D. Leparoux, "The potential of seismic methods for detecting cavities and buried objects: Experimentation at a test site," *J. Appl. Geophys.*, vol. 56, pp. 93–106, 2004.
- [14] K. Sato, S. Akiba, Y. Kano, and K. Akatsu, "Estimation method of cavity below the road surface considering soundness of pavement of pavement for the heavy traffic road (in Japanese)," *J. Jpn. Soc. Civil Eng. Ser. E1*, vol. 71, no. 3, pp. I_135–I_143, 2015.
- [15] N. Kawamura and M. Tsubokawa, "Influence of void beneath asphalt pavement on FWD deflection (in Japanese)," *J. Jpn. Soc. Civil Eng. Ser. E1*, vol. 73, no. 3, pp. I_1–I_8, 2017.
- [16] T. Omar and M. L. Nehdi, "Remote sensing of concrete bridge decks using unmanned aerial vehicle infrared thermography," *Automat. Construction*, vol. 83, pp. 360–371, 2017.
- [17] C. Maierhofer *et al.*, "Application of impulse-thermography for non-destructive assessment of concrete structures," *Cement Concrete Composites*, vol. 28, pp. 393–401, 2006.
- [18] D. H. Chen and T. Scullion, "Detecting subsurface voids using ground-coupled penetrating radar," *Geotechnical Testing J.*, vol. 31, no. 3, pp. 217–224, 2008.
- [19] N. J. Cassidy, R. Eddies, and S. Dods, "Void detection beneath reinforced concrete sections: The practical application of ground-penetrating radar and ultrasonic techniques," *J. Appl. Geophys.*, vol. 74, no. 4, pp. 263–276, 2011.
- [20] F. Soldovieri, A. Brancaccio, G. Prisco, G. Leone, and R. Pierri, "A Kirchhoff-based shape reconstruction algorithm for the multimomostatic configuration: The realistic case of buried pipes," *IEEE Trans. Geosci. Remote Sens.*, vol. 46, no. 10, pp. 3031–3038, Oct. 2008.

- [21] P. Gamba and S. Lossani, "Neural detection of pipe signatures in ground penetrating radar images," *IEEE Trans. Geosci. Remote Sens.*, vol. 38, no. 2, pp. 790–797, Mar. 2000.
- [22] W. Al-Nuaimy, Y. Huang, M. Nakhkash, M. T. C. Fang, V. T. Nguyen, and A. Eriksen, "Automatic detection of buried utilities and solid objects with GPR using neural networks and pattern recognition," *J. Appl. Geophys.*, vol. 43, pp. 157–165, 2000.
- [23] J. Sonoda and T. Kimoto, "Experimental images identification with simulation images and finetuning for objects identification of ground penetrating radar using deep learning (in Japanese)," in *Proc. Annu. Conf. Jpn. Soc. Artif. Intell.*, Jun. 2018, Art. no. 3Z2-03.
- [24] J. Sonoda and T. Kimoto, "Underground model inversion for GPR images by deep learning using generative adversarial networks (in Japanese)," *IEICE Trans. Electron. C*, vol. J104–C, no. 3, pp. 60–66, 2021.
- [25] T. Yamaguchi, T. Mizutani, and T. Nagayama, "Mapping subsurface utility pipes by 3-D convolutional neural network and kirchhoff migration using GPR images," *IEEE Trans. Geosci. Remote Sens.*, vol. 59, no. 8, pp. 6525–6536, Aug. 2021.
- [26] K. Belli, C. M. Rappaport, H. Zhan, and S. Wadia-Fascetti, "Effectiveness of 2-D and 2.5-D FDTD ground-penetrating radar modeling for bridge-deck deterioration evaluated by 3-D FDTD," *IEEE Trans. Geosci. Remote Sens.*, vol. 47, no. 11, pp. 3656–3663, Nov. 2009.
- [27] T. Wang and M. L. Oristaglio, "3-D simulation of GPR surveys over pipes in dispersive soils," *Geophysics*, vol. 65, no. 5, pp. 1560–1568, 2000.
- [28] T. H. Friis, "A note on a simple transmission formula," *Proc. IRE*, vol. 34, no. 5, pp. 254–256, 1946.
- [29] Nvidia, "GEFORCE GTX 1080 ti," USA. Accessed: Nov. 1, 2021. [Online]. Available: www.nvidia.com/en-gb/geforce/products/10series/geforce-gtx-1080-ti/#
- [30] K. Kamnitsas *et al.*, "Efficient multi-scale 3D CNN with fully connected CRF for accurate brain lesion segmentation," *Med. Image Anal.*, vol. 36, pp. 61–78, 2017.
- [31] S. Ji, W. Xu, M. Yang, and K. Yu, "3D convolutional neural networks for human action recognition," *IEEE Trans. Pattern Anal. Mach. Intell.*, vol. 35, no. 1, pp. 221–231, Jan. 2013.
- [32] K. Simonyan and A. Zisserman, "Very deep convolutional networks for large-scale image recognition," in *Proc. Int. Conf. Learn. Representations*, May 2015.
- [33] C. Szegedy *et al.*, "Going deeper with convolutions," in *Proc. IEEE Conf. Comput. Vis. Pattern Recognit.*, Jun. 2015, pp. 1–9.
- [34] N. Srivastava, G. Hinton, A. Krizhevsky, I. Sutskever, and R. Salakhutdinov, "Dropout: A simple way to prevent neural networks from overfitting," *J. Mach. Learn. Res.*, vol. 15, pp. 1929–1958, 2014.
- [35] I. Goodfellow, Y. Bengio, and A. Courville, *Deep Learning*, 1st ed. Cambridge, MA, USA: MIT Press, 2016.
- [36] T. Yamaguchi, "Automatic 3-D localization of utility pipes and void from ground penetrating radar signals by deep learning and digital signal processing," Doctoral dissertation, Univ. Tokyo, Tokyo, Japan, 2020.
- [37] J. Davis and M. Goadrich, "The relationship between precision-recall and ROC curves," in *Proc. Int. Conf. Mach. Learn.*, Jun. 2006, pp. 233–240.
- [38] J. M. Lobo, A. Jimenez-Valverde, and R. Real, "AUC: A misleading measure of the performance of predictive distribution models," *Glob. Ecol. Biogeography*, vol. 17, pp. 145–151, 2008.
- [39] W. H. Hayt, *Engineering Electromagnetics*, 1st ed. New York, NY, USA: McGraw-Hill, 1979.
- [40] N. R. Replinski, F. T. Ulaby, and M. C. Dobson, "Dielectric properties of soils in the 0.3–1.3 GHz range," *IEEE Trans. Geosci. Remote Sens.*, vol. 33, no. 3, pp. 803–807, May 1995.
- [41] C. Warren, A. Giannopoulos, and I. Giannakis, "gprMax: Open source software to simulate electromagnetic wave propagation for ground penetrating radar," *Comput. Phys. Commun.*, vol. 209, pp. 163–170, 2016.
- [42] J. P. Berenger, "A perfectly matched layer for the absorption of electromagnetic waves," *J. Comput. Phys.*, vol. 114, pp. 185–200, 1994.
- [43] K. S. Yee, "Numerical solution of initial boundary value problems involving maxwell's equations in isotropic media," *IEEE Trans. Antennas Propag.*, vol. 14, no. 3, pp. 302–307, May 1966.
- [44] U. Böniger and J. Tronicke, "Subsurface utility extraction and characterization: Combining GPR symmetry and polarization attributes," *IEEE Trans. Geosci. Remote Sens.*, vol. 50, no. 3, pp. 736–746, Mar. 2012.
- [45] A. Shaari, R. S. Ahmad, and T. H. Chew, "Effects of antenna-target polarization and target-medium dielectric contrast on GPR signal from non-metal pipes using FDTD," *NDT E Int.*, vol. 43, no. 5, pp. 403–408, 2010.
- [46] K. Iizuka, A. P. Freundorfer, K. H. Wu, H. Mori, H. Ogura, and V. K. Nguyen, "Step frequency radar," *J. Appl. Phys.*, vol. 56, no. 9, pp. 2572–2583, 1984.
- [47] Google, "TensorFlow," USA. Accessed: Nov. 1, 2021. [Online]. Available: www.tensorflow.org
- [48] J. L. Volakis, *Antenna Engineering Handbook*, 1st ed. New York, NY, USA: McGraw-Hill, 2007.



Takahiro Yamaguchi (Member, IEEE) was born in Tokyo, Japan, in 1991. He received the B.S., M.S., and the Ph.D. degrees in civil engineering from the University of Tokyo, Tokyo, Japan, in 2015, 2017, and 2020, respectively.

He is currently a Project Researcher with the Institute of Industrial Science (IIS), the University of Tokyo, Tokyo, Japan. His research interests include automatic and real time assessment of asphalt pavement, bridge decks, tunnels and subsurface conditions by digital signal processing, image processing, inverse analysis, machine learning and deep learning of radar, laser signals and dynamic responses.



Tsukasa Mizutani (Member, IEEE) was born in Osaka, Japan, in 1983. He received the B.S. degree in urban engineering, and the M.S. and Ph.D. degrees in civil engineering from the University of Tokyo, Tokyo, Japan, in 2007, 2009, and 2011, respectively.

He was an Assistant Professor with the Department of Civil Engineering, School of Engineering, the University of Tokyo, from 2011 to 2017. He was a Project Lecturer with the Institute of Industrial Science (IIS), the University of Tokyo, from 2017 to 2019, and has been an Associate Professor with IIS since 2019. His

research interests include digital signal processing, and electromagnetic wave measurement for structural health monitoring.

Dr. Mizutani was the recipient of the 2020 ASCE Moisseiff Award, and the 2020 Prize for Science and Technology (Young Scientist Category), the Commendation for Science and Technology by the Minister of Education, Culture, Sports, Science, and Technology in Japan.



Kimiro Meguro was born in Fukushima, Japan, in 1962. He received the Ph.D. degree in civil engineering from the University of Tokyo (UTokyo), Tokyo, Japan, in 1991.

He joined the Institute of Industrial Science, UTokyo, as a Research Associate. He became a Professor in 2004. His research interests include disaster management from structural to nonstructural measures, such as development of numerical tools for the analysis of total collapse behavior of structures, development of seismic retrofit method for weak structures in developing countries and its promotion systems, disaster information system, policy-making for disaster management.

Dr. Meguro was the recipient of many awards from academic organizations and has been serving Presidents of the Japan Society for Natural Disaster Science, Institute of Social Safety Science, Japan Association of Earthquake Engineering, and Special Advisor of Cabinet Office, Japanese Government, etc.



Takuichi Hirano (Senior Member, IEEE) was born in Tokyo, Japan, on January 28, 1976. He received the B.S. degree in electrical and information engineering from the Nagoya Institute of Technology, Nagoya, Japan, in 1998, and the M.S. and D.E. degrees in electrical and information engineering from the Tokyo Institute of Technology, Tokyo, Japan, in 2000 and 2008, respectively.

He was an Assistant Professor with the Tokyo Institute of Technology from 2002 to 2018. He is currently an Associate Professor with Tokyo City University,

Tokyo. His research interests include electromagnetic theory, numerical analysis for EM problems, and antenna engineering.

Mr. Hirano was the recipient of the Young Engineer Award from the IEICE Japan in 2004, the IEEE AP-S Japan Chapter Young Engineer Award in 2004, and the IEEE MTT-S Japan Chapter Young Engineer Award in 2011.